Membrane conductance of an electroporated cell analyzed by submicrosecond imaging of transmembrane potential

Masahiro Hibino,* Masaya Shigemori,‡ Hiroyasu Itoh,§ Kuniaki Nagayama,‖ and Kazuhiko Kinosita, Jr.*

*Department of Physics, Faculty of Science and Technology, Keio University, Hiyoshi, Kohoku-ku, Yokohama-shi, Kanagawa 223; ‡Department of Physics, Faculty of Science, Gakushuin University, Mejiro, Toshima-ku, Tokyo 171; §Tsukuba Research Laboratory, Hamamatsu Photonics K. K., Tokodai, Toyosato-machi, Tsukuba-shi, Ibaragi 300-26; ‖Biometrology Lab, JEOL Ltd., Nakagami, Akishima-shi, Tokyo 196, Japan

ABSTRACT Transmembrane potential was induced in a sea urchin egg by applying a microsecond electric pulse across the cell. The potential was imaged at a submicrosecond time resolution by staining the cell membrane with the voltage-sensitive fluorescent dye RH292. Under moderate electric fields, the spatial distribution of the induced potential as well as its time dependence were in accord with the theoretical prediction in which the cell membrane was regarded as an insulator. At higher field intensities, however, the potential apparently did not fully develop and tended to saturate above a certain level. The saturation is ascribed to the introduction of a large electrical conductance, in the form of aqueous openings, in the membrane by the action of the induced potential (electroporation). Comparison of the experimental and theoretical potential profiles indicates that the two regions of the membrane that opposed the electrodes acquired a high membrane conductance of the order of 1 S/cm^2 within 2 μs from the onset of the external field. The conductance was similar in the two regions, although permeability in the two regions of the membrane long after the pulse treatment appeared quite different.

INTRODUCTION

Electroporation is the phenomenon in which a cell exposed to an electric pulse is permeabilized as though aqueous pores are introduced in the cell membrane (see, e.g., Zimmermann, 1982; Tsong, 1983; Neumann et al., 1989). The phenomenon offers a means of artificially manipulating cellular contents, thereby serving as a useful tool in cell biology and cell technology. The molecular mechanism of the permeabilization process, however, is not yet fully understood.

The direct cause of electroporation has been suggested to be the large transmembrane potential induced by the externally applied electric field. If so, poration is expected only in those regions of the cell membrane that oppose the electrodes where the magnitude of the induced potential is large. Electroporation is a fast process that takes place in the micro- or submicrosecond time range (Kinosita and Tsong, 1977*c*, 1979). Thus the analysis of electroporation requires a spatial resolution of submicrometer and a time resolution of submicrosecond.

In previous reports (Kinosita et al., 1988*a*, *b*) we have shown that a pulsed-laser fluorescence microscope with a submicrosecond imaging capability offered the required spatial and temporal resolutions. Transmembrane potential induced in a sea urchin egg was visualized with a voltage-sensitive fluorescent dye. Electroporation was detected as a decrease in the potential caused by the ionic current flowing through the pores. Here we extend these studies and give a detailed account of the analysis of the membrane conductance that arises as a result of electroporation.

Address correspondence to Dr. K. Kinosita, Jr.

MATERIALS AND METHODS

Samples

Unfertilized eggs were obtained from sea urchins *Hemicentrotus pulcherrimus, Temnopleurus toreumaticus, Anthocidaris crassispina, Scaphechinus mirabilis,* or the sand dollar *Clypeaster japonicus.* No systematic differences in the results were found among these species, except for the variation in the resistance to damage following electroporation: as described below, an egg electroporated under moderate conditions recovered within 2 s and gave an apparently similar response when the pulse treatment was repeated. The most severe conditions that the egg could stand, however, varied depending on the species and season.

The eggs were washed and suspended in one of the following media. Calcium-free sea water was prepared by adding 1 mM $MgSO_4$ and 1 mM EGTA (ethylenebis-[oxyethylenenitrilo]tetraacetic acid) to Ca, Mg-free sea water (Jamarine Laboratories, Inc., Osaka, Japan). Isotonic low-salt media were prepared by mixing 0.55 M KCl and 0.9 M glucose and then adding 1 mM $MgSO_4$ and 0.1 mM Tris (tris-[hydroxymethyl]aminomethane). All solutions were titrated to pH 7.8 with KOH. The jelly coat on the eggs disappeared during the washing procedure. Conductivity of the suspending medium was measured with a conductivity meter (model CM-1K; Toa Denpa Co., Ltd., Tokyo).

Before the eggs were placed on the microscope stage they were resuspended in the same medium containing 2 μM RH292 (*N*-[3-(triethylammonium)propyl]-4-[4-(*p*-dibutylaminophenyl) butadienyl]-pyridinium dibromide; Molecular Probes, Inc., Eugene, OR) for 1–2 min and then washed once in the dye-free medium. Fluorescence imaging was made within 10 min after the staining.

All procedures were carried out at room temperature (22 ± 2°C).

0006-3495/91/01/209/12 $2.00

Induction of membrane potential

A suspension of sea urchin eggs stained with the voltage sensitive dye RH292 was placed between a pair of rectangular platinized-platinum electrodes, as described by Kinosita et al. (1988*b*). The gap between the electrodes was 1 mm wide, and its top and bottom were bounded by a pair of coverglasses leaving a gap height of 0.1 mm.

A home-made programmable pulse generator delivered a square-wave electric pulse(s) to the electrodes. The generator could produce two independent sets of pulses, each with a desired delay with respect to a trigger input. Each set consisted of zero to any number of pulses with a desired amplitude (up to ±150 V, 50 mA), polarity (fixed or alternating), duration, and interval. These parameters were set by digital switches, which allowed rapid resetting during an experiment. In high voltage experiments in sea water, the output of the generator was amplified with a booster amplifier with a maximal current output of 1 A (model 4015; NF Electronics Instruments Co., Ltd., Yokohama, Kanagawa, Japan).

The voltage and current across the sample were monitored on a digital storage oscilloscope (model DS-6121; Iwatsu Co., Ltd., Tokyo) through a circuit similar to one described in Kinosita and Tsong (1977*a*). The rise and fall times of the pulses were 1 μs in the worst case.

Pulsed-laser fluorescence microscope

Fig. 1 shows a block diagram of the pulsed-laser fluorescence microscope. A rotatable mirror was placed in the excitation path of an inverted epifluorescence microscope (ICM-405; Carl Zeiss Co., Ltd., Tokyo) so that its excitation source could be switched from an ordinary mercury lamp to a pulsed dye laser. The laser (DL-1400; Phase-R, New Durham, NH) delivered light pulses of 0.3 μs duration at a wavelength of 540 nm at a repetition rate of 0.5 Hz. The laser beam was enlarged with a beam expander so as to fill the entire field diaphragm in the excitation path. The beam was attenuated with neutral density filters so that the light level at the sample stage was <1 mJ/pulse. The beam was blocked with a solenoid-driven shutter until a measurement cycle was initiated. When a sea urchin egg stained with RH292 was placed on the stage and the shutter was opened, fluorescence images flashing at 0.5 Hz, each lasting for only 0.3 μs, could be seen with the naked eye through the eye piece.

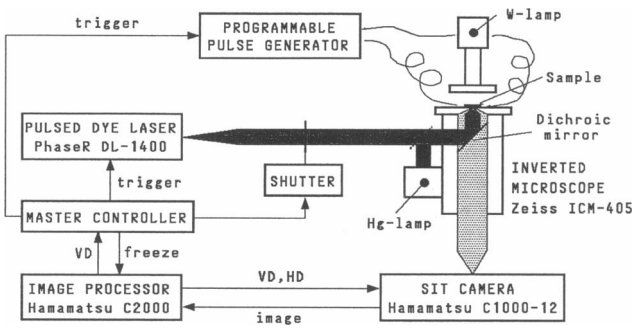

FIGURE 1 Block diagram of the pulsed-laser fluorescence microscope. The image processor provides video synchronization signals VD and HD, vertical and horizontal deflection pulses, to the camera. In the master controller the VD at 30 Hz is reduced to 0.5 Hz and sent, after a delay, to the external trigger input of the pulsed laser. When the controller is activated into the "measure" mode the selected VD is also sent to the image processor to initiate the freezing operation and to the programmable pulse generator to stimulate the sample. The shutter is opened in the "measure" mode. Peripherals to the image processor include a console terminal, a printer, image monitors (color, and black and white), hard and floppy disk drives, an optical disk drive (for mass storage), a video hardcopy system (Polaroid and 35 mm, model HC-1000; Toshiba Co., Ltd., Fukaya, Saitama, Japan), and a video tape recorder (NV-FS1000; Matsushita Electronics Co., Ltd., Osaka, Japan).

The flashing fluorescence images (above 600 nm, viewed through a 40× objective) were recorded with a video camera (SIT type C1000-12; Hamamatsu Photonics K. K., Hamamatsu, Shizuoka, Japan) for subsequent analysis. The laser was triggered during the vertical blanking period of the camera. The 0.3 μs image produced by the laser excitation was captured and held on the target plate of the camera until read out by electrical scanning at the normal video rate of 1 frame per 33 ms (noninterlace mode). The output of the camera was digitized (8 bits) and stored in a frame memory (16-bit, 512 × 480 pixels per page) of the image processor (C2000, Hamamatsu Photonics K. K.). Because the SIT camera showed considerable image lag (a fading image persisted in subsequent frames), for each image 16 consecutive frames were accumulated in the same page of the frame memory.

In one measurement, seven or eight different images, each acquired at 2 s intervals, were taken into different pages of the frame memory. First the laser was turned on and run at 0.5 Hz. The clock triggering the laser was obtained by selecting every 2 s a vertical deflection (VD) signal which was synchronous with the vertical blanking period of the camera. Then the shutter was opened, and the selected VD was fed to the programmable pulse generator which in turn delivered an electric pulse(s) to the sample. The selected VD was also sent to the image processor to command image freezing. In between laser pulses, the pulse generator was reset manually for a different stimulus condition, and the frame memory page was advanced by one. After the series of 7 or 8 imagings the shutter was closed and the laser turned off. In some cases signal averaging was attempted by repeating the series several times and accumulating the images on top of the previous ones. The results reported below, however, are based on single shot images except where stated otherwise.

Image analysis

From an acquired image a dark image was subtracted consisting mainly of the electrical noise of the camera. This resultant image was then spatially filtered twice (average over 3 × 3 pixels).

For quantitative analysis of the fluorescence image a "ring profile" was calculated. As shown in Fig. 2 the image of a stained egg appeared as a ring because the fluorescence of the dye adsorbed on the cell membrane was integrated at the outer edge of the image where the cell surface was perpendicular to the image plane. The intensity profile was thus calculated along this ring. First a pair of concentric circles were positioned on the image so that they sandwich the ring image (dashed lines in Fig. 2). The region between the circles was divided into trapezoids by equally spaced radii (10° intervals in Fig. 2; one trapezoid shown at the top). Then the average intensity in a trapezoid was calculated by averaging intensity values of the brightest pixels in that trapezoid. The number of pixels counted in each trapezoid was the arc length times the "thickness" of the image ring, both in pixel units. The thickness was somewhat arbitrarily chosen to be four pixel units for the egg images with a diameter of ~100 pixels; the average intensity was not very sensitive to the thickness. The ring profile was obtained by

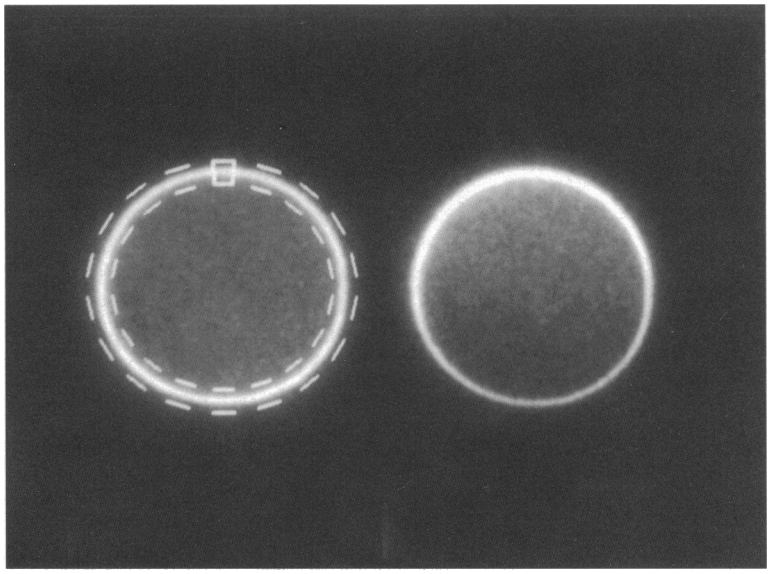

FIGURE 2 Fluorescence images of a sea urchin egg in the absence (*left*) and presence (*right*) of an electric field (100 V/cm, direction from top to bottom). The field was applied for 10 μs in calcium-free sea water and the image at right was taken at 8 μs. The dashed concentric circles on the image at left illustrate the way the ring profile is calculated (see Methods).

linearly interpolating the trapezoid intensity values. The profile thus had a limited angular resolution (10° except where stated otherwise).

Finally the intensity profile was converted into one representing the fractional fluorescence change. Of the series of seven or eight images obtained from one sample, the first and last were usually taken in the absence of the applied electric field. When the intensity profiles of these two reference images coincided with each other, the whole measurement was judged satisfactory and the two profiles were averaged to yield a reference profile. All other profiles were then divided by the reference profile so that the final ring profile represented the fractional change in fluorescence intensity. This procedure eliminated slight distortions resulting from the spatial inhomogeneity in laser illumination, camera sensitivity, and dye staining. In the division the shot-to-shot fluctuation in laser intensity (normally a few percent) was also corrected for by scaling by a constant factor. The factor was determined by assuming that the applied field should not influence the fluorescence intensity at the equator of the cell ($\theta = 90°$ in Fig. 4).

Note, in the above, that we compared several images in a measurement only when the first and last reference images were the same: we wanted to make sure that later images did not suffer from repeated electric-pulse treatments. This was particularly important in electroporation experiment because poration by one electric pulse occasionally led to dye penetration into the cell interior by the time the second electric pulse was applied. The resultant change in dye distribution distorted the fluorescence profile. When we applied several porating pulses to one sample, the test was usually more stringent: two identical electric pulses with an intensity below the critical value for poration were applied at the beginning and end, and the responses were required to be the same. Severe electroporation for which apparent recovery by 2 s was no longer observed could only be studied through comparison of many independent samples. Results reported below were obtained under relatively mild conditions and passed the above test.

RESULTS AND DISCUSSION

Fluorescence response to a subcritical electric pulse

In Fig. 2 we compare two fluorescence images of an egg stained with RH292, in the absence (*left*) and 8 μs after the onset (*right*) of an electric field at 100 V/cm. The image at left appears as a uniform ring, indicating homogeneous staining. Upon the application of the electric field the fluorescence intensity on the positive-electrode side (*top*) increased whereas on the negative-electrode side (*bottom*) it decreased. The fractional change in fluorescence intensity, together with the changes under different field intensities, are plotted in Fig. 3 in the form of the ring profiles. The profiles in *a* are noisy because they were calculated at an angular resolution as small as 2°, from single-shot images. This noise, however, could be considerably reduced by applying the same electric field 20 times and accumulating the resultant images (Fig. 3 *b*).

Grinvald et al. (1982) have shown that the fluorescence intensity of RH292 changes linearly with the membrane potential. We therefore interpret the fluorescence changes shown in Figs. 2 and 3 as representing the transmembrane potential induced across the cell membrane of the egg by the externally applied electric field. Theoretically, the potential $\Delta\Psi$ induced in a spherical

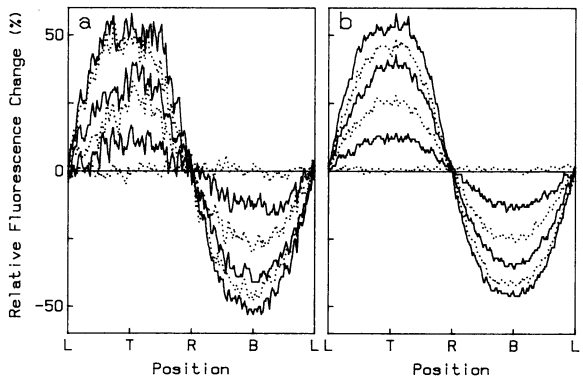

FIGURE 3 Field-induced changes in the fluorescence intensity of RH292 staining the surface of a sea urchin egg. The ring profiles were calculated as described in Methods at an angular resolution of 2° from single-shot images (*a*) or from images accumulated over 20 shots under the same electric field (*b*). The six profiles with an increasing amplitude in each panel show the responses under field intensity of 0, 25, 50, 75, 100, and 125 V/cm. The six images for *a* were taken in this order, and then the six for *b* were accumulated while this sequence was repeated 20 times on the same egg. All images were taken at 8 μs in a 10-μs electric pulse. The profile at 100 V/cm in *a* corresponds to the image at the right in Fig. 2. *T*, top of the image (positive-electrode side); *R*, right; *B*, bottom (negative-electrode side); *L*, left.

cell of radius a by an external field E_0 (see Fig. 4) is given by

$$\Delta\Psi = 1.5aE_0 \cos\theta\,[1 - \exp(-t/\tau)] \quad (1)$$

$$\tau = aC(r_i + r_e/2), \quad (2)$$

where t is the time after the field is turned on, C is the membrane capacitance per unit area, and r_i and r_e are specific resistances of the intra- and extracellular media (Cole, 1972). Note that $\Delta\Psi$ in our notation is $\Psi_e - \Psi_i$ whereas physiological potentials, for which Ψ_e is constant, are usually defined as $\Psi_i - \Psi_e$. For the data at t = 8 μs in Figs. 2 and 3, the exponential term in Eq. 1 should be negligible because τ is calculated, and experimentally confirmed, to be ~1 μs for the egg in high-salt (≳100 mM) media (Kinosita et al., 1988*a*).

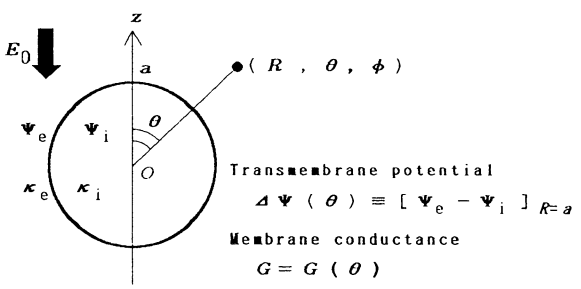

FIGURE 4 Definition of symbols. *O*, center of the cell; *a*, radius of the cell; E_0, applied electric field; Ψ_e and Ψ_i, electrical potential outside and inside the cell; κ_e and κ_i, extra- and intracellular conductivity; (R, θ, φ), polar coordinates with respect to the z-axis.

The ring profiles in Fig. 3 resemble cosine curves, suggesting that the observed signals are in fact approximately proportional to the induced potential, $\Delta\Psi$. The time dependence of the fluorescence signal was also in accord with Eqs. 1 and 2. This was confirmed in media of various ionic strengths which gave a range of τ values between 1 and 15 μs (data not shown; examples in Kinosita et al., 1988*a*, *b*). The cosine dependence of the field-induced $\Delta\Psi$ was first demonstrated by Gross et al. (1986), also using a voltage-sensitive dye (di-4-ANEPPS), under steady-state conditions at low field intensities. Using the same dye Ehrenberg et al. (1987) have demonstrated the exponential time dependence (Eq. 1) and the linear dependence of τ on r_e (Eq. 2).

In Fig. 5 the fractional fluorescence change at $\theta = 0°$ is plotted against the field intensity, E_0. A linear dependence would be expected from Eq. 1, but the observed fluorescence signal started to saturate at $E_0 \sim \pm 100$ V/cm. Within this range the signal was roughly proportional to E_0. Because the egg had a radius of 50 μm, $\Delta\Psi(\theta = 0°, t = \infty)$ is calculated to be 0.75 V at E_0 = 100 V/cm. The fractional change in fluorescence in the approximately linear range is therefore 50–70% per volt for the data obtained upon excitation at 540 nm (○ and ●). For physiological potentials, Grinvald et al. (1982) obtained a fluorescence intensity change of −7% per

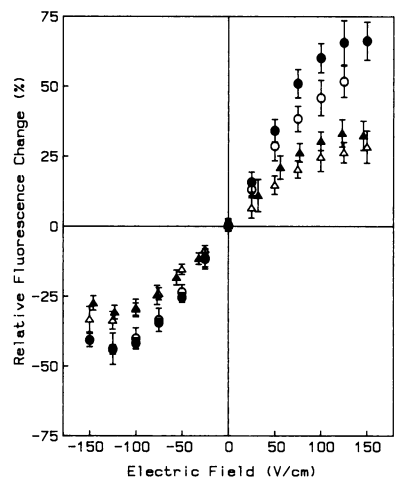

FIGURE 5 Dependence of the fluorescence signal on the field intensity. ○ and ●, excitation at 540 nm; △ and ▲, at 520 nm. From single-shot images obtained in calcium-free sea water the ring profiles at 10° resolution were calculated. The profile values at $\theta = 0°$ are plotted on the right-hand side and the values at $\theta = 180°$ on the left. Each data point represents the average and standard deviation over five to eight measurements on different eggs. Filled and closed symbols were obtained on different days.

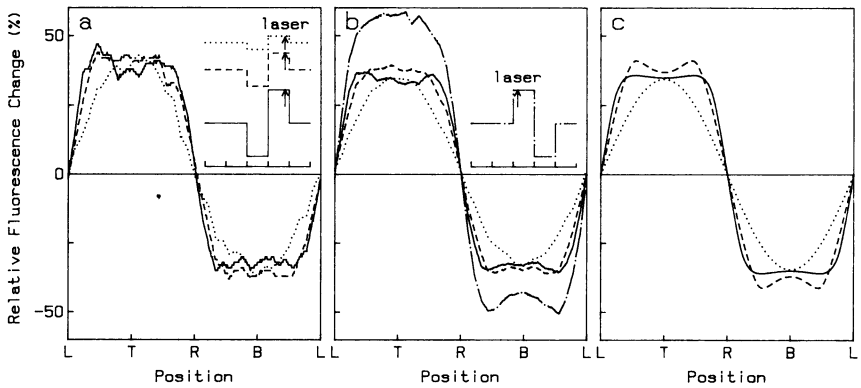

FIGURE 6 (*a*) Fluorescence changes under supracritical electric fields. The ring profiles were calculated at an angular resolution of 10° from single-shot images taken at 18 μs in a symmetrical reversing electric pulse (first half, duration 10 μs with the direction from bottom to top; second half, 10 μs from top to bottom; see inset). An egg in calcium-free sea water was treated with a series of four reversing pulses with amplitudes of 80 V/cm (*dotted line*), 186 V/cm (*dashed line*), 400 V/cm (*solid line*), and again 80 V/cm (*not shown*); ring profiles for the first and last pulses agreed within experimental error. (*b*) Averaged profiles obtained from eight independent measurements, of which *a* is one, on eight different eggs. The chain line is the profile at 2 μs in the first half of a reversing pulse of 400 V/cm (eight eggs different from those for the other profiles were used). (*c*) Theoretical potential profiles for a spherical cell with a finite membrane conductance given in Eq. 3. (*Dotted line*) $G_0 = 0$; (*dashed line*) $\theta_c = 44°$ and $G_0 = 1.8$ S/cm^2; (*solid line*) $\theta_c = 70°$ and $G_0 = 4.3$ S/cm^2. The parameter $\nu \equiv \kappa_i/\kappa_e$ defined in the Appendix is taken as 0.1. The potential value is scaled so that the height of the reference profile (*dotted line*) is approximately equal to the experimental one in *b*.

100 mV (−100 mV in our notation) for RH292 on cultured cells (excitation at 546 nm). Our results appear consistent with theirs both in magnitude and sign.

The saturation of the fluorescence response above 100 V/cm (see Fig. 6 for high field data) can be accounted for by either of the following two effects. One is that $\Delta\Psi$ deviates from Eq. 1 and shows saturation as a result of electroporation which is expected to take place at $|\Delta\Psi| \sim 1$ V. The other possibility is a nonlinear response of the dye fluorescence to $\Delta\Psi$. While the dye response cannot be precisely linear over a wide range of $\Delta\Psi$, as may be evident already in the small asymmetry around the origin in Fig. 5, we consider that the major cause of the saturation is electroporation. One reasoning for this assumption is that the saturation started on both sides of the cell (positive and negative E_0-axes in Fig. 5) at about the same field intensity.[1] This is an expected behavior for electroporation (see below), but nonlinearity of the dye response is likely to be asymmetric because this dye supposedly responds to signed $\Delta\Psi$ and not to $|\Delta\Psi|$. For example, part of the mechanism by which styryl dyes, of which RH292 is one, respond to potential has been shown to be electrochromism, or a shift of the absorption spectrum (Loew and Simpson, 1981). Then the magnitude as well as linearity of the response would depend on the position of the excitation wavelength relative to the spectrum. As is shown in Fig. 5, the observed fluorescence response was much smaller with excitation at 520 nm (△ and ▲), yet the saturation field intensity appears unchanged. In a medium of low ionic strength (1 mM KCl) the peak of corrected excitation spectrum of RH292 on the egg was at 500 nm compared with 530 nm in calcium-free sea water (data not shown). Excitation at 540 nm in the low-salt medium gave a fluorescence response (Kinosita et al., 1988*b*) which was more asymmetric (positive signal larger than negative) than that shown in Fig. 5. There again the saturation took place at about the same field intensity. These observations support, although do not prove, our contention that the saturation is essentially that of $\Delta\Psi$. Changes in the disposition of the dye in the membrane in response to a large $|\Delta\Psi|$ might lead to a symmetric saturation in the dye response. Polarized fluorescence images, however, indicated that at least the dye orientation relative to the membrane normal was not significantly altered by the applied electric field (unpublished observations).

[1]Strictly, the actual membrane potential is the sum of the induced potential in Eq. 1 and the resting potential of the unfertilized egg. The latter has been reported to be 60–80 mV, inside negative (Hagiwara and Jaffe, 1979). In Fig. 5, therefore, the total potential becomes zero at the abscissa value of ~ −9 V/cm. In the present work we neglect the resting potential because its magnitude is much smaller than that of the induced potential.

Electroporation

The critical membrane potential above which electroporation occurs is ~ 1 V for most cell membranes (Zimmermann, 1982; Tsong, 1983). The findings of Baker et al. (1980) suggest a similar value for the cell membrane of

sea urchin eggs: treatment with an exponentially decaying electric pulse with a decay time constant of 125 μs rendered the eggs permeable to Ca^{2+} when the peak amplitude exceeded 100 V/cm. This field intensity would induce a maximal transmembrane potential of 1.1 V in their eggs with a diameter of 150 μm. The eggs that we used had a diameter of ~100 μm and for these the critical voltage of 1 V is attained at the field intensity of 133 V/cm. In fact we noticed a morphological change in the egg surface after the eggs were exposed to a square-wave electric pulse of amplitude 150 V/cm and duration 100 μs in normal sea water. Under higher field this change took the form of partial elevation of the fertilization envelope, indicating the entry of Ca^{2+} into the egg. No such changes were observed in Ca^{2+}-free sea water.

The saturation seen in Fig. 5 is thus an expected result of electroporation: once the membrane is porated, further increase in $\Delta\Psi$ is counteracted by the ionic current through the pores. The saturation is more clearly shown in Figs. 6, *a* and *b*, where the ring profiles obtained under supracritical fields are seen to be flat or even slightly concave at the top and bottom. The most straightforward interpretation is that these regions of the cell, where $|\Delta\Psi|$ calculated from Eq. 1 would have exceeded the critical value of ~1 V, were porated to such an extent that $|\Delta\Psi|$ was reduced below the critical value. In the following arguments we adopt this view and assume that the fluorescence signal is approximately proportional to $\Delta\Psi$ even when the ring profile shows a flat top and bottom. In Fig. 6 *b*, for example, we directly compare the flat profiles with the reference profile at E_0 = 80 V/cm (*dotted line*), and estimate $|\Delta\Psi|$ in the flat regions of the solid and dashed profiles to be ~0.6 V, the value for $\Delta\Psi(\theta = 0°, E_0 = 80$ V/cm) in Eq. 1. The validity of this assumption is re-examined at several points below.

To compare with Fig. 7, the profiles in Figs. 6, *a* and *b*, except the chain line in Fig. 6 *b*, were taken at 18 μs in a symmetric reversing electric pulse with a total width of 20 μs. The profile at 2 μs in a 400 V/cm pulse is also shown in Fig. 6 *b* in chain line. This profile at 2 μs is already highly saturated at the top and bottom: $|\Delta\Psi|$ estimated as above is ~1 V, whereas Eq. 1 predicts 2.6 V (for τ = 1 μs). Profiles recorded at 8 μs (not shown) were also saturated and quite similar to those at 18 μs, except that $|\Delta\Psi|$ in the flat regions was higher by ~0.05 V. It appears that the cell membrane cannot sustain a voltage difference >1 V even for a period as short as 2 μs. When the membrane potential reaches the critical value of ~1 V, the membrane is porated and starts to conduct ionic current. The membrane conductance will immediately rise to a level which is sufficient to keep $|\Delta\Psi|$ below the critical value. Thereafter, the further increase in the conductance is rather slow on the microsecond time scale, resulting in the gradual decrease in $|\Delta\Psi|$ described above. Conductivity measurements with erythrocyte suspensions (Kinosita and Tsong, 1979) have suggested a similar time course for erythrocyte electroporation.

The above interpretation based on the assumed proportionality between the fluorescence signal and $\Delta\Psi$ is in accord with the observation of Coster and Zimmermann (1975). These authors directly injected current

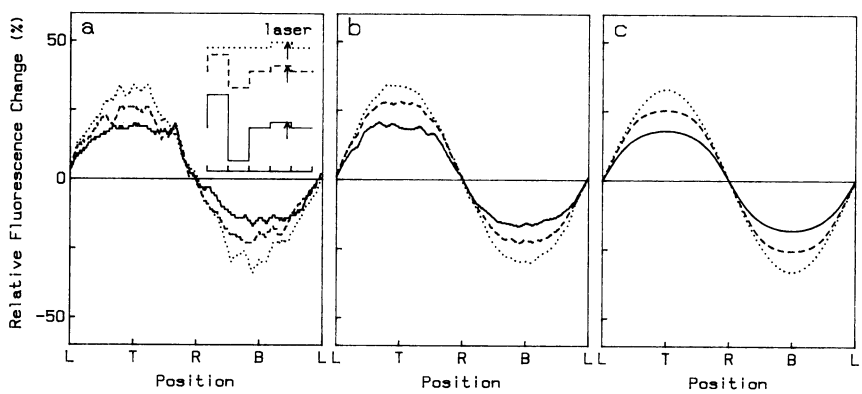

FIGURE 7 (*a*) Fluorescence changes observed under a small monitor pulse with and without a preceding supracritical pulse. Ring profiles at 10° resolution from single-shot images at 8 μs in a 67 V/cm pulse. (*Dotted line*) Without a preceding pulse; (*dashed line*) 10 μs after a reversing 186 V/cm pulse; (*solid line*) 10 μs after a reversing 400 V/cm pulse (*see inset*). An egg in the calcium-free sea water was exposed to a series of four pulse sequences, three in the above order and the last without the preceding pulse; the first and last profiles agreed with each other. (*b*) Averaged profiles obtained from eight measurements, of which *a* is one, on eight different eggs. (*c*) Theoretical potential profiles. (*Dotted line*) G_0 = 0; (*dashed line*) $\theta_c = 44°$ and $G_0 = 0.5$ S/cm^2; (*solid lines*) $\theta_c = 70°$ and $G_0 = 1.0$ S/cm^2. $\nu \equiv \kappa_i/\kappa_e = 0.1$. The height of the dotted profile is adjusted to approximate the experimental profile in *b*.

into a cell of *Valonia utricularis* and measured the membrane potential using intracellular electrodes. When the potential augmented by the current exceeded a critical value of ~1 V, a dramatic increase in the membrane conductance took place, which was just large enough to keep the potential at the critical value. When the current was held constant after this "breakdown," a gradual decrease in the potential on the microsecond time scale was observed, implying a gradual increase in membrane conductance.

Whereas the gradual decrease in the profile height (the difference between 2 and 18 μs profiles in Fig. 6 *b*) is consistent with the electroporation kinetics, the saturation of dye response by itself does not predict this behavior. The decrease could have been due to redistribution or reorientation of the dye in the sustained field. However, both intensity and polarization of the RH292 fluorescence 10 μs after the termination of the electric pulse were indistinguishable from those before the pulse.

The more or less symmetric flattening of the ring profiles, even under a unidirectional electric field, is also reasonable if it reflects a symmetric poration. As discussed in the Appendix, poration on only one side of the cell will immediately (well within τ in Eq. 2) double the membrane potential on the opposite side. One side poration is thus very unlikely. Once both sides are porated, any further increase in the membrane conductance on the two sides will also tend to be matched because otherwise the less conducting side would experience a higher membrane potential. Note, however, that the symmetrical increase in the membrane conductance during the pulse treatment does not necessarily leave the two sides of the cell equally permeable after the external field is removed. There have been reports in which influx or efflux of substances into or out of a cell that had been porated was observed on only one side of the cell (Rossignol et al., 1983; Mehle et al., 1985; Sowers, 1988). We also noticed that the treatment of an egg with a supracritical pulse in normal sea water produced a partial fertilization envelope only on the negative-electrode side, or else the envelope was greater on the negative side than on the positive side. Visualization of intracellular Ca^{2+} with a fluorescent indicator dye (unpublished observations) confirmed that Ca^{2+} influx into the electroporated egg was larger on the negative-electrode side than on the positive-electrode side.

An aftereffect of a supracritical pulse

If electroporation really underlies the saturation of the fluorescence signal, one expects to see some aftereffects of a supracritical electric pulse because the pores do not close immediately at the end of the pulse. To see if aftereffects existed we designed the pulse sequence shown in the inset of Fig. 7 *a*. First, a supracritical reversing pulse, similar to one used in Fig. 6, was given. Then, after an intermission of 10 μs, a subcritical pulse followed, during which the fluorescence signal was imaged. This image was compared with the image taken in the same subcritical pulse without the preceding supracritical pulse. Any difference between the two images would thus indicate an aftereffect of the supracritical pulse. The first pulse was given as a reversing pulse for the technical reason: in highly conductive sea water, a large rectangular pulse trailed a faint current tail which lasted for many microseconds. Platinization of the electrodes greatly reduced, but did not completely eliminate, this tail. The tail produced a small electric field which acted as a nonzero baseline for the second pulse. Though this effect was small, we chose to eliminate the tail completely by reversing the first pulse.

The ring profiles in Figs. 7, *a* and *b*, are the fluorescence responses to the subcritical pulse with and without the preceding supracritical pulse. Compared with the reference profile obtained in the absence of the preceding pulse, the other two are lower in amplitude, clearly demonstrating an expected aftereffect. Our interpretation is that the large membrane conductance introduced by the preceding pulse still remained at a high level when the second pulse was applied. Because the three profiles in Fig. 7 *b* (and in 7 *a*) are fluorescence signals obtained under identical electric pulses, we consider the differences among the three to be the strongest support for our interpretation of the fluorescence signal in terms of electroporation.[2] Rigorously, though, we cannot exclude the possibility that even this aftereffect seen in Figs. 7, *a* and *b*, is also an intrinsic property of the fluorescent dye. If so, it would mean that the behavior of the dye coincides with the expected features of electroporation in every aspect so far examined.

[2]As mentioned at the end of Image Analysis, severe electroporation often resulted in dye penetration into the egg. After the penetration the dye response (fractional fluorescence change) apparently became smaller because the dye on the intracellular surface of the membrane contributed a response with the opposite sign. The penetration was an irreversible phenomenon, and was immediately noticeable because the fluorescence intensity in the penetrated area became higher than before. The results reported in Fig. 7 were obtained under milder conditions and are free from the dye penetration effect: the fluorescence intensity returned to the initial value after the electric field was removed (confirmed 2 s, and also 10 μs, after the termination of the electric pulse). Moreover, the aftereffect disappeared after the intermission of 2 s (the dotted profile was recovered; see legend to Fig. 7). This last observation indicates rapid recovery of porated membrane after the field was removed.

Estimation of membrane conductance

Below we attempt a semi-quantitative analysis of the fluorescence signal in terms of the membrane conductance. To do so we assume, as already stated above, that the observed fluorescence change is approximately proportional to $\Delta\Psi$ even when the fluorescence profile shows a flat top and bottom: we interpret the flat $\Delta\Psi$ as arising from finite membrane conductance introduced by the electropores. Specifically we assume that the membrane conductance $G(\theta)$ is of the form:

$$G(\theta) = \begin{cases} G_0 \dfrac{(|\cos\theta| - \cos\theta_c)}{(1 - \cos\theta_c)} & (0° \leqq \theta \leqq \theta_c, \\ & \quad 180° - \theta_c \leqq \theta \leqq 180°) \\ 0 & (\theta_c < \theta < 180° - \theta_c). \end{cases} \quad (3)$$

Eq. 3, chosen arbitrarily without compelling reason, implies that the conductance introduced is proportional to the excess potential, i.e., $|\Delta\Psi|$ that would be obtained in the absence of pores minus the critical potential for poration: θ_c is the angle at which $|\Delta\Psi|$ in the absence of pores equals the critical potential. Our goal is to estimate G_0, the maximal membrane conductance attained at the two poles ($\theta = 0°$ and 180°). As shown in the Appendix, once we assume the form of $G(\theta)$, we can generate a set of theoretical curves for $\Delta\Psi$ for different values of G_0. Comparison with experimental $\Delta\Psi$ then allows the estimation of G_0.

The theoretical curves that appear to simulate the experimental results are shown in Figs. 6 *c* and 7 *c*. To calculate these curves we assumed that the critical potential was 1 V, i.e., $\theta_c = 70°$ at $E_0 = 400$ V/cm and $\theta_c = 44°$ at $E_0 = 186$ V/cm. We also used a measured value for r_e, the specific resistance of the calcium-free sea water, of 20 Ω·cm, and an assumed value for r_i, the specific resistance of the cell interior, of 200 Ω·cm (Hiramoto, 1959). Uncertainty exists in these values (except for r_e), but we are not attempting precise analysis because the experimental $\Delta\Psi$ estimated from the fluorescence is already very approximate. Calculations in the Appendix suggest that when $r_i > r_e$, it is mainly the product of G_0 and r_i that determines the values of $\Delta\Psi$ in the flat regions (with the terminology in the Appendix, g_0 determines $\Delta\psi$ when $\nu < 1$; see Figs. A2 and A3). The estimated G_0 value should therefore be of the right order of magnitude.

From Figs. 6, *b* and *c*, G_0 at 18 μs in the applied field is estimated to be ~4.3 S/cm² at $E_0 = 400$ V/cm, and ~1.8 S/cm² at 186 V/cm. If the membrane conductance of 4.3 S/cm² is attributed to aqueous pores of length 10 nm, the fraction of membrane area occupied by the pores is calculated to be between 0.1 and 0.01%, corresponding to pores filled with the intracellular medium or with sea water, respectively. Similar values were obtained in media of low ionic strengths (Kinosita et al., 1988*a*, *b*). The membrane conductance in electroporated erythrocytes has also been estimated, from conductivity measurement with cell suspensions, to be of similar order of magnitude both at high and low ionic strengths (Kinosita and Tsong, 1979). Although the membrane conductance in the presence of the applied field appears to be rather insensitive to the ionic strength, the size of individual pores that remain open long after the field is removed has been shown to be much larger at low ionic strengths (Kinosita and Tsong, 1977*b*, *c*). The kinetics of membrane recovery may be highly dependent on the ionic strength.

After the intermission of 10 μs, the membrane conductance was reduced to below one third: from Figs. 7, *b* and *c*, G_0 after a pulse of 400 V/cm is estimated to be ~1.0 S/cm², and after the 186 V/cm pulse, ~0.5 S/cm². The recovery of the porated membrane is rapid, as has already been shown for erythrocytes (Kinosita and Tsong, 1979). After a 2-s intermission, we no longer detected finite membrane conductance: ring profile indistinguishable.

The experimental and theoretical curves in Figs. 6 and 7 are in good agreement. This implies that the assumed form of $G(\theta)$ reflects the essential feature of the actual membrane conductance. The membrane conductance cannot be too highly concentrated at the poles (a single large pore at each pole) because that would result in a deep depression of $\Delta\Psi$ at the poles (see the curve for $\theta_c = 15°$ in Fig. A4 in the Appendix). Nor can the conductance be evenly distributed over the whole cell surface because then the ring profile would be a cosine with a reduced amplitude. In Fig. 6 *b* the flat regions in the profile are wider at 400 V/cm than at 186 V/cm, implying that only those regions where $\Delta\Psi$ exceeded the critical value were porated. Comparison with Fig. A5 in the Appendix also suggests that the form of $G(\theta)$ in Eq. 3 is an appropriate choice: the degree of poration is highest at the poles ($\theta = 0°$ or 180°) and gradually decreases toward the periphery.

CONCLUSION

We have interpreted the saturation of the fluorescence signal from a membrane-bound potential-sensitive dye as representing the saturation of membrane potential due to electroporation. The results of the analysis are consistent with known and/or anticipated features of electroporation. The analysis, in particular, has allowed the estimation of membrane conductance while the

membrane is porated. In the presence of a supracritical electric field, those regions of the cell membrane which would experience a supracritical potential, irrespective of its sign, appear to be porated within microseconds to a high level, equivalent to the replacement of 0.01 ~ 0.1% of the membrane area by aqueous openings. The temporal and spatial resolution provided by the current approach should prove useful in revealing the still unclear mechanism of electroporation.

APPENDIX

Transmembrane potential for finite membrane conductance

Here we calculate theoretical membrane potential for a spherical cell with a finite membrane conductance placed in a homogeneous electric field. We ignore the initial transients during the onset of the field, and deal with the steady state. Then the electrical potentials inside and outside the cell, Ψ_i and Ψ_e, satisfy Laplace's equation

$$\nabla^2\Psi_i = \nabla^2\Psi_e = 0 \tag{A1}$$

with boundary conditions

$$\Psi_e \to E_0 R\cos\theta \text{ as } R \to \infty \tag{A2}$$

$$\kappa_i[\partial\Psi_i/\partial R]_{R=a} = \kappa_e[\partial\Psi_e/\partial R]_{R=a} \tag{A3}$$

$$= G[\Psi_e - \Psi_i]_{R=a}, \tag{A4}$$

where E_0 is the intensity of the electric field far from the cell, κ_i and κ_e are the conductivities of the intra- and extracellular media, a is the cell radius (membrane thickness ignored), G is the membrane conductance, and (R, θ, ϕ) are the polar coordinates (Fig. 4). The condition A2 states that the electric field far from the cell is homogeneous and in the direction toward $-z$. Eqs. A3 and A4 represent the continuity of current at the cell surface, the right-hand side of Eq. A4 being the transmembrane current.

Introduction of the following dimensionless quantities

$$\psi_i \equiv \Psi_i/aE_0,\ \psi_e \equiv \Psi_e/aE_0,\ r \equiv R/a,$$
$$\nu \equiv \kappa_i/\kappa_e,\ g \equiv (a/\kappa_i)G$$

converts Eqs. A1–A4 to

$$\nabla^2\psi_i = \nabla^2\psi_e = 0 \tag{A5}$$

$$\psi_e \to r\cos\theta \text{ as } r \to \infty \tag{A6}$$

$$[\partial\psi_i/\partial r]_{r=1} = (1/\nu)[\partial\psi_e/\partial r]_{r=1} \tag{A7}$$

$$= g[\psi_e - \psi_i]_{r=1}. \tag{A8}$$

If we assume that g is symmetric around the z-axis, i.e., $g = g(\theta)$, then ψ's are also symmetric around the z-axis. Then Eqs. A5–A7 are satisfied by ψ's of the following form:

$$\psi_i = c_0 + \sum_{n=1}^{\infty} \frac{c_n r^n P_n(\cos\theta)}{n} \tag{A9}$$

$$\psi_e = \left[r + \frac{1}{2r^2}\right] P_1(\cos\theta) - \nu\left[\sum_{n=1}^{\infty} \frac{c_n P_n(\cos\theta)}{(n+1)r^{n+1}}\right], \tag{A10}$$

where P_n is the Legendre polynomial of order n, and c_n's are constants. Note that the term c_0/r is absent in Eq. A10 because otherwise net current flows into or out of the cell violating the steady state condition. If g is symmetric with respect to the x-y plane, i.e., $g(\theta) = g(180° - \theta)$, c_0 in Eq. A9 also disappears:

$$c_0 = 0. \tag{A11}$$

Below we assume this symmetry except where stated otherwise.

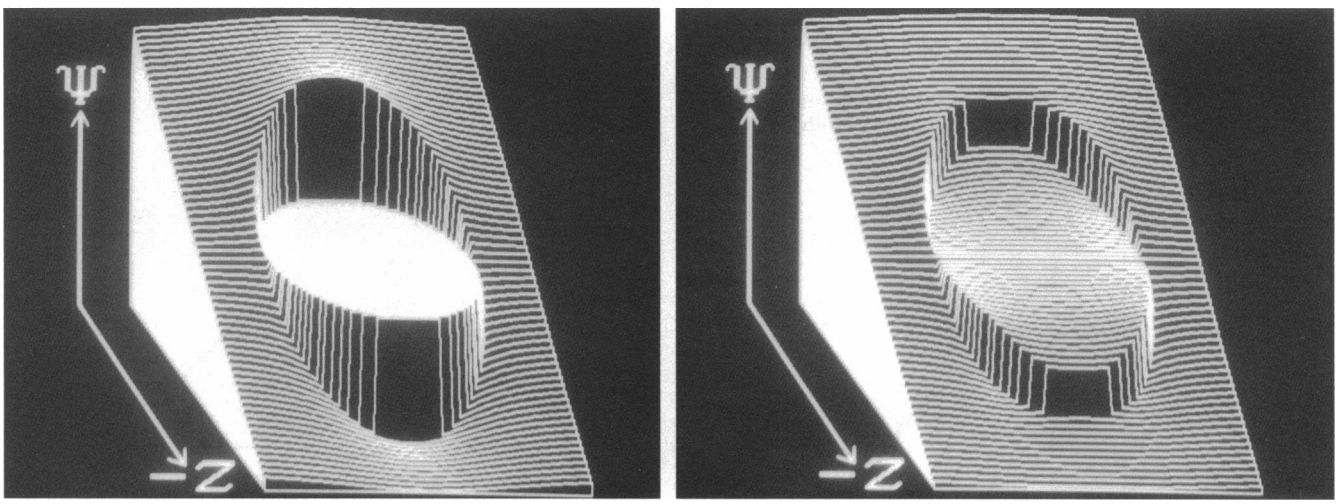

FIGURE A1 Potential profiles around a cell exposed to an external electric field. The profiles represent potential values in a plane containing the center of the cell and the field axis ($-z$). (*Left*) A cell with negligible membrane conductance; (*right*) a cell with a finite membrane conductance given by Eq. A16 ($j = 1$, $\theta_c = 45°$, $g_0 = 2$, $\nu \equiv \kappa_i/\kappa_e = 1$).

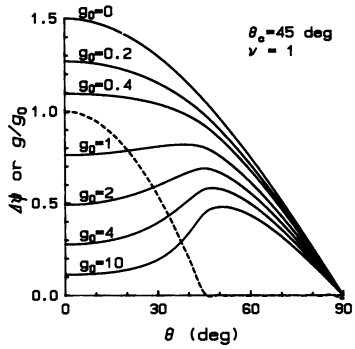

FIGURE A2 Reduced transmembrane potential $\Delta\psi \equiv \Delta\Psi/aE_0$ (*solid lines*) for different values of membrane conductance. Theoretical values obtained numerically for conductance given by Eq. A16 with $j = 1$, $\theta_c = 45°$, $\nu \equiv \kappa_i/\kappa_e = 1$. Dashed lines (all superimposed on top of each other) represent the form of the truncated membrane conductance (Eq. A15) which is an approximation to Eq. A16 but for which the potential values (*solid lines*) are exact. See text for details.

Introduction of Eqs. A9 and A10 into A8 gives

$$\sum_{n=1}^{\infty} c_n P_n(\cos\theta) = g(\theta)\left\{\frac{3}{2}P_1(\cos\theta) - \sum_{n=1}^{\infty} c_n\left[\frac{\nu}{n+1}+\frac{1}{n}\right]P_n(\cos\theta)\right\}. \quad \text{(A12)}$$

Multiplying both sides of Eq. A12 by $P_m(\cos\theta)$ and integrating over θ = 0° to 180°, we obtain

$$\frac{2}{2m+1}c_m = \frac{3}{2}g_{m1} - \sum_{n=1}^{\infty} c_n\left[\frac{\nu}{n+1}+\frac{1}{n}\right]g_{mn}, \quad \text{(A13)}$$

where

$$g_{mn} = \int P_m(\cos\theta)g(\theta)P_n(\cos\theta)\, d\cos\theta. \quad \text{(A14)}$$

Eqs. A13 for $m = 1 \ldots \infty$ constitute a linear equation system for c_n's. Under the assumed symmetry, in particular, only c_n's with odd n are to be considered.

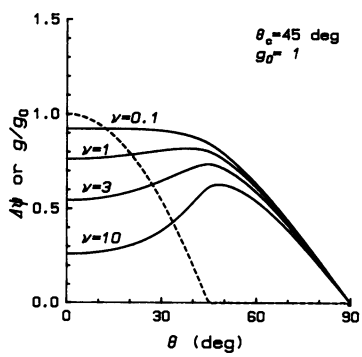

FIGURE A3 Reduced transmembrane potential for different ν. See legend to Fig. A2.

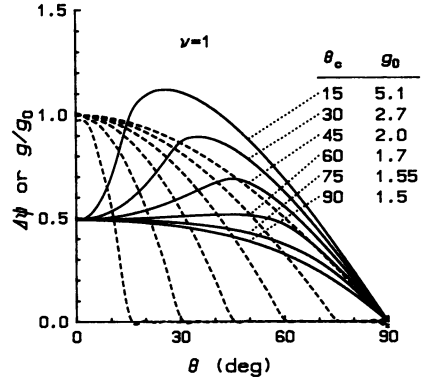

FIGURE A4 Reduced transmembrane potential for different θ_c. The conductance values (g_0) are so chosen that all curves have approximately the same height at $\theta = 0°$. See legend to Fig. A2.

For practical purposes the summations can be truncated at $n = N$. Then Eqs. A13 for $m = 1 \ldots N$ can be solved numerically by computer. The integration in Eq. A14 can also be performed numerically. The truncated solution thus obtained is an approximation to the exact solution for the given $g(\theta)$. From the derivation, however, one sees that the truncated solution is the exact solution for $g^{(t)}(\theta)$ given by

$$g^{(t)}(\theta) = [\partial\psi_i^{(t)}/\partial r]_{r=1}/[\psi_e^{(t)} - \psi_i^{(t)}]_{r=1}, \quad \text{(A15)}$$

where (t) denotes the truncated solutions. We found, as long as $g(\theta)$ changes smoothly, $g^{(t)}(\theta)$ for $N = 59$ was sufficiently close to $g(\theta)$. Curves $g(\theta)$ in Figs. A2–A5, as well as $G_m(\theta)$ in Kinosita et al. (1988*a*, *b*), represent this $g^{(t)}(\theta)$.

In the following we present several numerical results for $g(\theta)$ of the form

$$g(\theta) = \begin{cases} g_0 \dfrac{(|\cos\theta| - \cos\theta_c)^j}{(1-\cos\theta_c)^j} & (0° \leqq \theta \leqq \theta_c, \\ & 180° - \theta_c \leqq \theta \leqq 180°) \\ 0 & (\theta_c < \theta < 180° - \theta_c), \end{cases} \quad \text{(A16)}$$

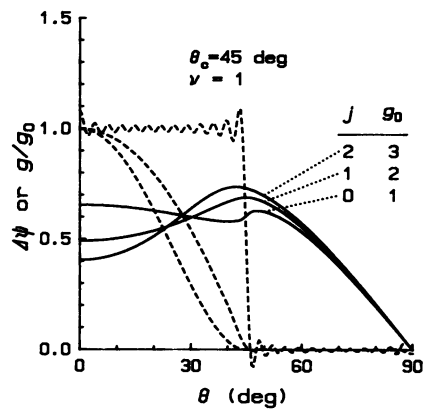

FIGURE A5 Reduced transmembrane potential for different shape of membrane conductance. The conductance values are so chosen that the total conductance [$g(\theta)$ integrated over the cell surface] is the same for all three cases. See legend to Fig. A2.

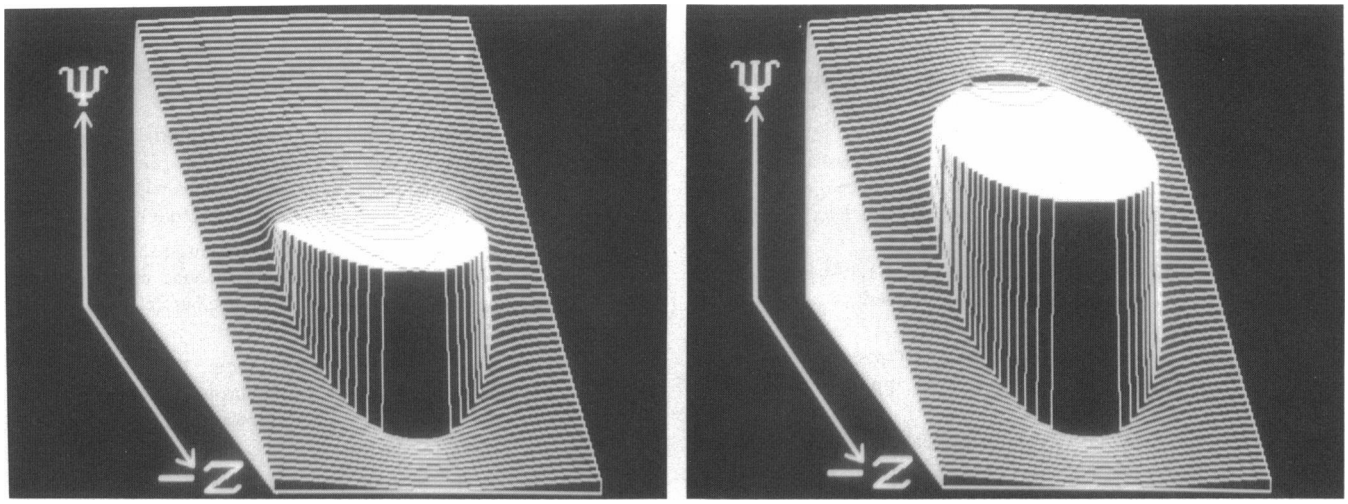

FIGURE A6 Potential profiles around a cell porated on one side. The profiles represent potential values in a plane containing the center of the cell and the field axis ($-z$). The membrane conductance on the negative-electrode side ($-z$) is zero, whereas that on the positive side ($+z$) is given by Eq. A16 in which $j = 0$, $\theta_c = 90°$, $g_0 = 100$, $\nu = 1$ (*left profile*), or $j = 1$, $\theta_c = 45°$, $g_0 = 2$, $\nu = 1$ (*right profile*). The profile at left corresponds to the extreme case where the positive half of the cell has disappeared. Calculated transmembrane potentials, in units of aE_0, are $\Delta\psi$ ($\theta = 0°$) = 0.01 and $\Delta\psi(\theta = 180°) = -1.95$. The profile at right is to be compared with the symmetrically porated case shown in Fig. A1, right. For the one-side poration shown here, $\Delta\psi$ ($\theta = 0°$) = 0.09 and $\Delta\psi(\theta = 180°) = -2.83$. Note that $\Delta\psi(\theta = 180°)$ for an unporated cell is -1.50. One-side poration always leads to a greater potential difference at $\theta = 180°$. Except for the extreme case of the total disappearance of the positive hemisphere, $\Delta\psi(\theta = 180°)$ is close to -3.

where $j = 0$, 1, or 2. The $g(\theta)$ in Eq. A16 is finite in the two regions near the poles, and its maximal value is g_0. In Fig. A1 are compared two potential profiles, one with $g_0 = 0$ and the other with $g_0 = 2$. The figure shows how the current passing through the cell, when the membrane conductance becomes finite, changes the potential distribution in and around the cell and reduces the transmembrane potential.

In Figs. A2–A5, solid lines represent the reduced transmembrane potential, $\Delta\psi \equiv [\psi_e - \psi_i]_{r=1}$, and dashed lines the normalized membrane conductance $g(\theta)/g_0$. Fig. A2 shows how $\Delta\psi$ changes with g_0 for the case of $j = 1$ (similar trends for $j = 0$ or 2), and Fig. A3 with $\nu = \kappa_i/\kappa_e$. Fig. A4 shows the dependence on θ_c (g_0 adjusted so that all curves in this figure have approximately the same height at $\theta = 0°$). Note that $\Delta\psi$ for small θ_c tends to be highly concave: a single pore of appreciable conductance at each pole will produce a very concave $\Delta\psi$. Fig. A5 shows that the basic feature of $\Delta\psi$ is relatively insensitive to j (shape of $g[\theta]$) except for $j = 0$ where an abrupt change in $g(\theta)$ occurs at $\theta = \theta_c$.

Finally we comment on the case where $g(\theta)$ is not symmetric across the x-y plane ($g[\theta] \neq g[180°–\theta]$). In this case c_0 in Eq. A9 remains finite. The value of c_0 is determined by the constraint that the transmembrane current (the left-hand side of Eq. A7) integrated over the cell surface should be zero. (After the onset of the external field a transient current flows until this condition is met.) Under this additional constraint Eqs. A13 for $m = 1 \ldots N$, with an additional term $-c_0 g_{m0}$ on the right-hand side, can be solved numerically (even m's and n's taken into account).

The case of interest is one in which only one side of the cell is porated. The potential distribution for this case can be inferred without recourse to the numerical solution (numerical analysis did confirm the following; see examples in Fig. A6). The potential inside the cell should be almost flat except for some undulation near the porated area. The potential outside the cell will not be very different from the potential in the absence of pores because the currents flowing into and out of the porated area should cancel with each other. This last reasoning also leads to the contention that the transmembrane potential in the porated region should, on the average, be small. Thus, one-side poration effectively brings the intracellular potential uniformly up to the value immediately outside the porated area. The transmembrane potential on the opposite side of the cell, then, almost doubles. An expected consequence is the immediate poration of the opposite side: one-side poration is unlikely except possibly for a very short period during the initial transient.

We thank Dr. A. Ikegami, Dr. Y. Inoue, and Dr. T. Hayakawa for their continuous support on which this work is based. Dr. T. Kouyama kindly allowed us to use his instruments. We also thank Drs. K. Hirano, I. Yasumasu, Y. Toyoshima, T. M. Noumura, Y. Tanaka, and I. Mabuchi for valuable suggestions and the help in obtaining sea urchins, and Mr. M. Hosoda for extensive support in developing the image-analysis system, and Drs. G. Marriott and G. Feigenson for critically reading the manuscript.

This work was supported by grants-in-aid from Ministry of Education, Science and Culture of Japan, and by Special Coordination Funds for Promoting Science and Technology from the Agency of Science and Technology.

Received for publication 2 May 1990 and in final form 6 July 1990.

REFERENCES

Baker, P. F., D. E. Knight, and M. J. Whitaker. 1980. The relation between ionized calcium and cortical granule exocytosis in eggs of the sea urchin Echinus esculentus. *Proc. Roy. Soc. Lond. B.* 207:149–161.

Cole, K. S. 1972. Membranes, Ions and Impulses. University of California Press, Berkeley, CA. 569 pp.

Coster, H. G. L., and U. Zimmermann. 1975. The mechanism of electrical breakdown in the membranes of *Valonia utricularis*. *J. Membr. Biol.* 22:73–90.

Ehrenberg, B., D. L. Farkas, E. N. Fluhler, Z. Lojewska, and L. M. Loew. 1987. Membrane potential induced by external electric field pulses can be followed with a potentiometric dye. *Biophys. J.* 51:833–837.

Grinvald, A., R. Hildesheim, I. C. Farber, and L. Anglister. 1982. Improved fluorescent probes for the measurement of rapid changes in membrane potential. *Biophys. J.* 39:301–308.

Gross, D., L. M. Loew, and W. W. Webb. 1986. Optical imaging of cell membrane potential changes induced by applied electric field. *Biophys. J.* 50:339–348.

Hagiwara, S., and L. A. Jaffe. 1979. Electrical properties of egg cell membranes. *Annu. Rev. Biophys. Bioeng.* 8:385–416.

Hiramoto, Y. 1959. Electric properties of Echinoderm eggs. *Embryologia.* 4:219–235.

Kinosita, K., Jr., and T. Y. Tsong. 1977*a*. Hemolysis of human erythrocytes by a transient electric field. *Proc. Natl. Acad. Sci. USA.* 74:1923–1927.

Kinosita, K., Jr., and T. Y. Tsong. 1977*b*. Formation and resealing of pores of controlled sizes in human erythrocyte membrane. *Nature (Lond.).* 268:438–441.

Kinosita, K., Jr., and T. Y. Tsong. 1977*c*. Voltage-induced pore formation and hemolysis of human erythrocytes. *Biochim. Biophys. Acta.* 471:227–242.

Kinosita, K., Jr., and T. Y. Tsong. 1979. Voltage-induced conductance in human erythrocyte membranes. *Biochim. Biophys. Acta.* 554:479–497.

Kinosita, K., Jr., I. Ashikawa, N. Saita, H. Yoshimura, H. Itoh, K. Nagayama, and A. Ikegami. 1988*a*. Electroporation of cell membrane visualized under a pulsed-laser fluorescence microscope. *Biophys. J.* 53:1015–1019.

Kinosita, K., Jr., I. Ashikawa, M. Hibino, M. Shigemori, H. Yoshimura, H. Itoh, K. Nagayama, and A. Ikegami. 1988*b*. Submicrosecond imaging under a pulsed-laser fluorescence microscope. *Proc. SPIE (Society of Photo-Optical Instrumentation Engineering).* 909:271–277.

Loew, L. M., and L. L. Simpson. 1981. Charge-shift probes of membrane potential. A probable electrochromic mechanism for *p*-aminostyrylpyridinium probes on a hemispherical lipid bilayer. *Biophys. J.* 34:353–365.

Mehle, W., U. Zimmermann, and R. Hampp. 1985. Evidence for asymmetrical uptake of fluorescent dyes through electro-permeabilized membranes of *Avena* mesophyll protoplasts. *FEBS (Fed. Eur. Biochem. Soc.) Lett.* 185:89–94.

Neumann, E., A. E. Sowers, and C. A. Jordan, editors. 1989. Electroporation and Electrofusion in Cell Biology. Plenum Publishing Co., New York. 436 pp.

Rossignol, D. P., G. L. Decker, W. J. Lennartz, T. Y. Tsong, and J. Teissie. 1983. Introduction of calcium-dependent, localized cortical granule break-down in sea-urchin eggs by voltage pulsation. *Biophys. Biochim. Acta.* 763:346–355.

Sowers, A. E. 1988. Fusion events and nonfusion contents mixing events induced in erythrocyte ghosts by an electric pulse. *Biophys. J.* 54:619–626.

Tsong, T. Y. 1983. Voltage modulation of membrane permeability and energy utilization in cells. *Biosci. Rep.* 3:487–505.

Zimmermann, U. 1982. Electric field-mediated fusion and related electrical phenomena. *Biochim. Biophys. Acta.* 694:227–277.